Supporting information for

Tungsten Oxide quantum dots-loaded Carbon Nitride Interlayer for Advancing Perovskite Solar Cells Performance

Zuhong Li [a,b], Li Zhao [b, *], Xiaojie Yang[c], Yanyan Li,[d] and Shimin Wang[a, *]

a Hubei Collaborative Innovation Center for Advanced Organic Chemical Materials, Ministry of Education Key Laboratory for the Green Preparation and Application of Functional Materials, School of Materials Science and Engineering, Hubei University, Wuhan 430062, PR China

b Dalian National Laboratory for Clean Energy, Dalian Institute of Chemical Physics, Chinese Academy of Sciences, Dalian 116023, PR China.

c School of Nuclear Technology and Chemistry & Biology, Hubei Key Laboratory of Radiation Chemistry and Functional Materials, Hubei University of Science and Technology, Xianning, Hubei 437100, China

d Key Laboratory of Textile Fiber and Products, Ministry of Education, Wuhan Textile University, Wuhan 430200, China

E-mail: zhaoli7376@163.com; shiminwang@126.com

Keywords: perovskite solar cells; quantum dots; carbon nitride; buried interfaces; SnO_2.

Experimental section

Materials and Reagents

Lead iodide (PbI_2, >99.99%), methylammonium iodide (MAI, >99.5%), and 2,2,7,7-tetrakis (N, N-di-p-methoxyphenyl-amine)9,9-spirobifluorene (Spiro-OMeTAD) were purchased from Xi'an Yuri Solar Co., Ltd. The solvents, including chlorobenzene (CB, 99.8%), iso-propanol (IPA), ethyl acetate, and acetonitrile (ACN) were purchased from Aladdin. N, N-dimethylformamide (DMF, ≥99.9%) and dimethyl-sulfoxide (DMSO, ≥99.9%) were purchased from J&K Scientific Ltd. Urea (99%) and $SnCl_2 \cdot 2H_2O$ (99.995%) were purchased from TCI Development Co. Thioglycolic acid, Bis(trifluoromethyl-sulfonyl)-imide lithium salt (Li-TFSI), Tris[4-(1,1-dimethylethyl)-2-(1H-pyrazol-1-yl)pyridine]cobaltsaltwith1,1,1-trifluoro-N-[(trifluoromethyl)sulfonyl]methanesulfonamide salt (FK209) and 4-tert-butyl pyridine (4-tBP) were purchased from Sigma-Aldrich. Gold (Au, 99.999%) pellets for electrode deposition were provided by Zhongnuo Advanced Material Technology. The FTO glass substrates (15 × 15 mm^2 with sheet resistance of 15 $Ohm \cdot sq^{-1}$) were purchased from Advanced Election Technology Co. Ltd. All of the other materials and solvents were purchased from Sinopharm Chemical Reagent Co. Ltd, without any further purification.

Preparation of precursor solutions

The WCN-x composite dispersions were prepared by mixing the aforementioned WO_3 QDs (0.05, 0.10, 0.20, and 0.30 $mg \cdot mL^{-1}$) and C_3N_3 aqueous dispersion (0.30 $mg \cdot mL^{-1}$) with equal volume ratios, and then stirred for 4 hours. Subsequently, these dispersions were diluted to 0.025, 0.05, 0.10, and 0.15 $mg \cdot mL^{-1}$, which were designated as WCN-2.5, WCN-5, WCN-10, and WCN-15, respectively. The preparation method of WCN-0 dispersion is the same as described above, where deionized water and C_3N_3 aqueous dispersion (0.30 $mg \cdot mL^{-1}$) are mixed in equal volume ratios, continuously stirred for 4 hours to obtain the WCN-0 composite dispersion with a C_3N_3 concentration of 0.15 $mg \cdot mL^{-1}$.

Perovskite precursor solution and film preparation

The 1.4M $(FAPbI_3)_{0.96}(MAPbBr_3)_{0.04}$ perovskite precursor was prepared by dissolving 705.35 mg PbI_2, 240.76 mg FAI, and 7.76 mg $MAPbBr_3$ in the mixture solvent of DMF and DMSO (volume ratio of 4:1). Then 13 mol% excess of PbI_2 and 50 mol% MACl were added into the precursor solution to stabilize the perovskite precursor. The solution was stirred overnight and subsequently filtered through a 0.22 μm Polytetrafluoroethylene (PTFE) filter prior to utilization. The filtered perovskite precursor was spin-coated onto the substrate at 1,000 rpm for 10 s and 5,000 rpm for 30 s; 100 μL of ethyl acetate as an anti-solvent were dripped onto the center of substrate at 10 s before the end of spin-coating. The as-prepared perovskite films were immediately annealed on a hotplate at 100 °C for 60 min.

The 1.5 M $MAPbI_3$ perovskite precursor solution was dissolved in DMF and DMSO (volume ratio of 9:1) with an equimolar molar ratio of MAI and PbI_2. The solution was stirred overnight and subsequently filtered through a 0.22 μm PTFE filter prior to utilization. The perovskite precursor was then spin-coated on the substrate by a two-consecutive step program at 1000 rpm for 6 s and 4000 rpm for 30 s; 100 μL CB was dripped on the substrate quickly at 16th s during the spin-coating program. Afterwards, the perovskite films were annealed on a hotplate at 100 °C for 15 min.

Device fabrication

The FTO glass substrates were sequentially cleaned by ultrasonication in detergent solution, followed by rinsing with ultrapure water, acetone, isopropanol, and ethanol for 20 min each. Then the substrates were dried under a nitrogen flow to remove excess solution and treated with UV-ozone for 25 min before use. The SnO_2 film was deposited on FTO substrates by chemical bath deposition (CBD) according to the previous reports.[1] Briefly, 650 μL of HCl (37 wt%), 12.5 μL of thioglycolic acid, 625 mg of urea, and 137.5 mg of $SnCl_2 \cdot 2H_2O$ were dissolved into 50 mL of deionized water in turn. The as-cleaned FTO glasses

were soaked into the preheated reaction mixture at 85 °C for 3.5 hours. The SnO_2 deposited FTO substrates were washed with deionized water and IPA, and subsequently annealed at 150 °C for 60 min in ambient air. After cooling to room temperature, the FTO/SnO_2 substrates were treated with UV-ozone for 15 min. For modified SnO_2 ETLs, the as-prepared WCN solutions were spin-coated onto the SnO_2 films at 4,000 rpm for 30 s with a ramp of 2000 rpm·s^{-1}, and followed by thermal annealing at 100 °C for 20 min to evaporate the solvent. After cooling the substrate to room temperature, it was treated with UV-ozone for 15 min and transferred to a nitrogen glove box. Perovskite solutions were deposited on the substrate as detailed above. The Spiro-OMeTAD solution was prepared by mixing 73 mg·mL^{-1} of Spiro-OMeTAD in 1 mL CB with 30 μL of 4-tBP, 18 μL of Li-TFSI (520 mg·mL^{-1} in ACN), and 29 μL of FK209 (375 mg·mL^{-1} in ACN), and then spin-coated on the top of the perovskite layer at 3,000 rpm for 30 s without thermal annealing. Finally, 80 nm thick of gold electrode was vapor-deposited on the substrate under high vacuum (less than 3×10^{-4} pa) via thermal evaporation technique; the evaporation speed was adjusted to 0.1 Å·s^{-1} for the first 5 nm, and then increased to 0.2 Å·s^{-1} from 5 to 15 nm, and finally reached 0.6 Å·s^{-1} for the rest of the procedure. The aperture area of each cell is 0.06 cm^2 using a metal shadow mask.

Characterizations Instrumentation

DLS measurements

Dynamic light scattering (DLS) measurements were conducted by using the HPPS5001 laser particle size analyzer from Malvern Instruments (United Kingdom) with a monochromatic coherent He–Ne laser (640 nm) as the light source. DLS measurements were carried out in WO_3 QDs, C_3N_3, and WCN solutions in deionized water to determine the particle size of micelles and the critical micelle concentration (CMC) of those materials in deionized water.

XRD measurements

X-ray diffraction (XRD) patterns were recorded over the 2θ range of 10º to 50º using a Bruker D8 Advance diffractometer (Germany), with operating parameters set to voltage values of 40 kV and current values of 40 mA, employing Cu-Kα radiation (λ=1.5418 Å).

FTIR measurements

Fourier-transform infrared (FTIR) spectra were acquired using the standard KBr disk method on a Nicolet iS10 spectrometer (USA).

UV-vis measurements

Ultraviolet-visible diffuse reflectance spectra (UV-vis DRS) measurements were conducted over the wavelength range of 300 to 900 nm using a Shimadzu UV-3600 spectrophotometer (Japan).

XPS and UPS measurements

Surface composition and chemical bonding states were analyzed via X-ray photoelectron spectroscopy (XPS) and ultraviolet photoelectron spectroscopy (UPS) using a Thermo Fisher Escalab-250Xi instrument (USA), equipped with Mg-Kα source, with the radiation source switched to He-Iα UV-light (21.22 eV), respectively.

SEM measurements

Morphology and structural features of both SnO_2 and perovskite films were characterized by Field-emission scanning electron microscopy (FESEM) using a

Zeiss Sigma 500 series (Germany).

TEM measurements

The characterization and chemical analysis of WO_3 QDs, C_3N_3, and WCN materials were characterized by a field emission transmission electron microscopy (TEM) using a Titan G2 60-300 (USA) equipped with an energy dispersive detector (EDS). This instrument offers a wide acceleration voltage range of 60-300 kV, achieving resolution at the atomic level.

AFM measurements

Atomic force microscopy (AFM) images were acquired using an Asylum Research MFP-3D system (USA).

Contact angles measurements

Water contact angles for SnO_2 and perovskite films were measured using the JC2000D1 contact angle goniometer manufactured by POWEREACH (China).

PL and TRPL measurements

Steady-state photoluminescence (PL) and time-resolved photoluminescence (TRPL) spectra were collected at room temperature using a FluoTime-300 fluorescence spectrometer (United Kingdom).

Photovoltaic measurements

Current density-voltage (*J-V*) characteristics were measured using a Keithley 2400 source meter under simulated AM 1.5 G solar illumination (100 $mW \cdot cm^{-2}$) provided by a Sirius-SS150A-D solar simulator (USA). The *J-V* curves were recorded over a voltage range from 1.2 V to -1.2 V at a scanning rate of 100 $mV \cdot s^{-1}$.

IPCE measurements

Incident photon-to-current conversion efficiency (IPCE) was evaluated over a wavelength range from 300 to 900 nm using a Newport TSL-300XU quantum efficiency measurement system (USA), operating in DC mode without bias light.

EIS measurements

Electrochemical impedance spectroscopy (EIS) measurements were employed

under the dark at an applied voltage of 1.0 V, utilizing a Zennium-IM6 electrochemical workstation (Germany) over a frequency range spanning from 2 MHz to 1 Hz.

Supplementary Note 1:

The synthetic route of WCN material was illustrated in Scheme S1. The preparation details were described as follows.

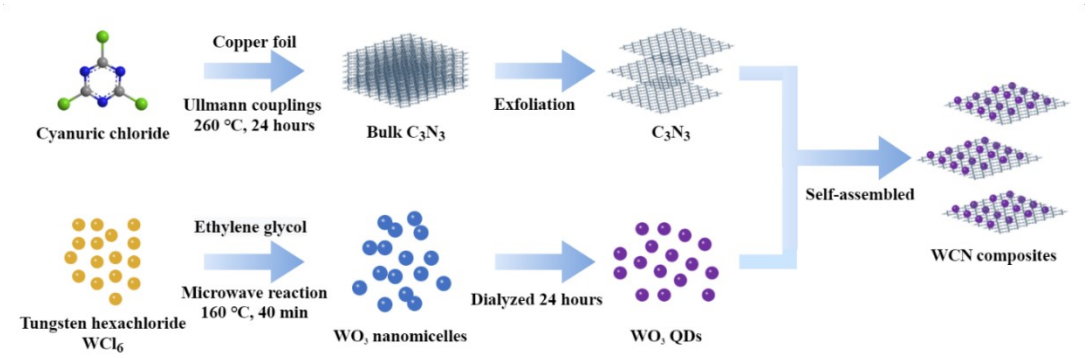

Scheme 1. Synthetic route of WCN composite material.

Synthesis of C_3N_3

The carbon nitride was synthesized following the methodology described in our previous publication.[2] In this study, Cyanuric chloride ($C_3N_3Cl_3$, 1600 mg) monomer and a fresh cleaned copper foil (0.05 mm thick) were introduced into a sealed reactor. Under the argon at 260 °C going a 24-hours reaction, resulting gray polymer film on the copper foil was carefully removed, and then ground in an agate mortar for 30 minutes. The obtained powder underwent multiple washes using deionized water, mixed acid (volume ratio of concentrated sulfuric and fuming nitric acid is 1:3) and absolute ethyl alcohol. The remaining product was then dried at 80 °C in a vacuum oven for at least 8 h, approximately 300 mg remained.

The carbon nitride (C_3N_3) aqueous dispersion (0.30 mg·mL^{-1}) was prepared by dispersing 30 mg of C_3N_3 powder into 100 mL of deionized water, followed by ultrasonic treatment for 4 to 6 hours at room temperature. Additionally, the solution was necessary ultrasonicated for 30 minutes to ensure uniform dispersion prior to use.

Synthesis of WO_3 QDs

The WO_3 QDs were prepared by a slight modification of a previously reported

method.[3] Typically, 100 mg of tungsten hexachloride (WCl_6) was dissolved into 10 mL of ethylene glycol and stirred continuously at room temperature until the solution becomes clear and transparent. The above solution was transferred to microwave reactor and reacted at 160 ℃ for 40 min. After natural cooling to room temperature, all the product-containing solution was filtered through a 0.22 μm microporous membrane to remove insoluble solid product. Based on the concentration difference on both sides of the dialysis bag, the concentrated solution was dialyzed in a dialysis bag (retained molecular weight of 3500) for 24 h with deionized water dialysis solvent to remove contamination and unfused small molecules. The concentration of WO_3 QDs aqueous solution was approximately 1.2 $mg \cdot mL^{-1}$.

The tungsten oxide quantum dots (WO_3 QDs) dilutions were prepared by diluting the original WO_3 QDs solution (1.2 $mg \cdot mL^{-1}$) with an appropriate amount of deionized water, obtaining in dilutions with different solid contents of 0.05, 0.10, 0.20, and 0.30 $mg \cdot mL^{-1}$, respectively.

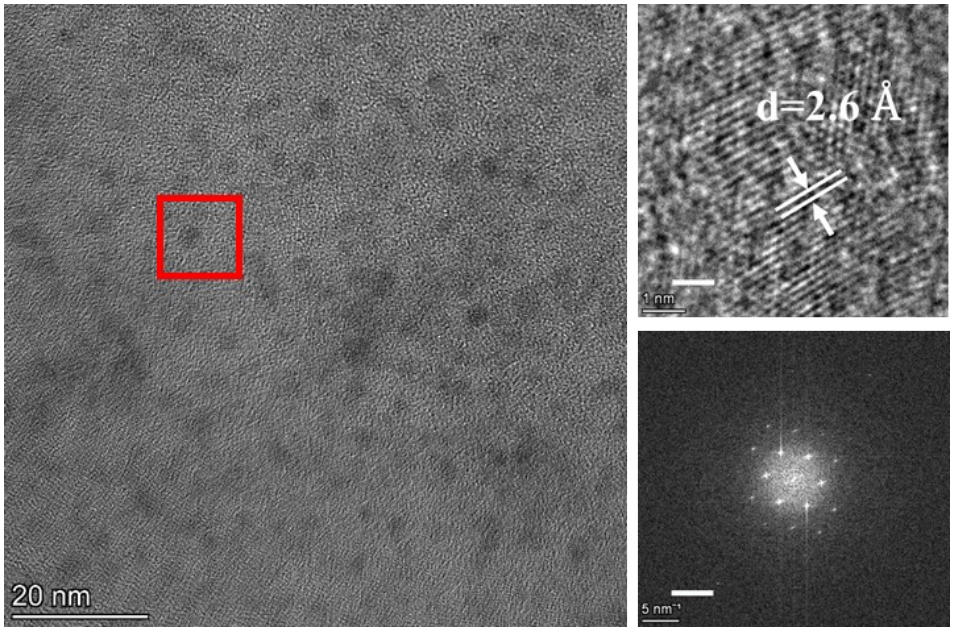

Figure S1. TEM image of WO_3 QDs material prepared by microwave synthesis process (scale bar: 20 nm), the high-resolution TEM image of WO_3 QDs material (scale bar: 1 nm) in the right inset, and selected area electron diffraction pattern of WO_3 QDs material (scale bar: 5 nm^{-1}) in the lower right inset. It reveals a lattice spacing of 2.6 Å, which corresponds to the (202) crystal plane of WO_3, indicating that the WO_3 QDs are well crystallized, with a uniform size from 4 to 7 nm, confirming the successful preparation of WO_3 QDs.

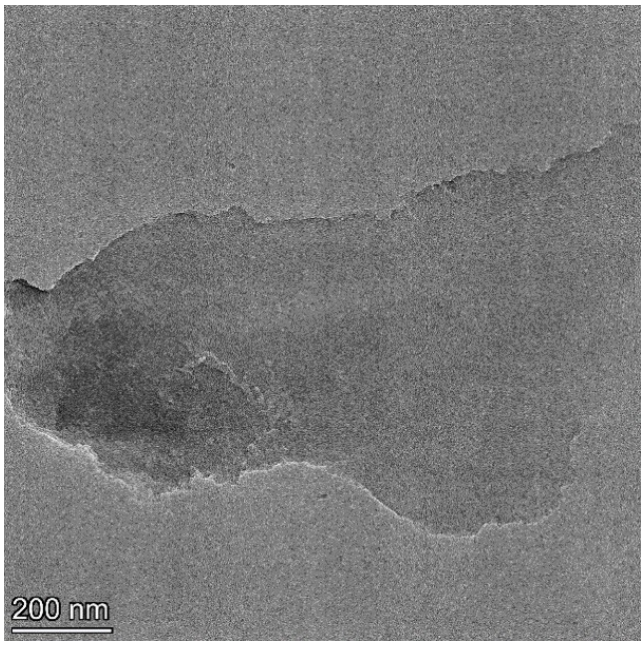

Figure S2. TEM image of WCN composite material, scale bar: 200 nm. The image disclosed wrinkled, veil-like nanosheets extending several hundreds of nanometers.

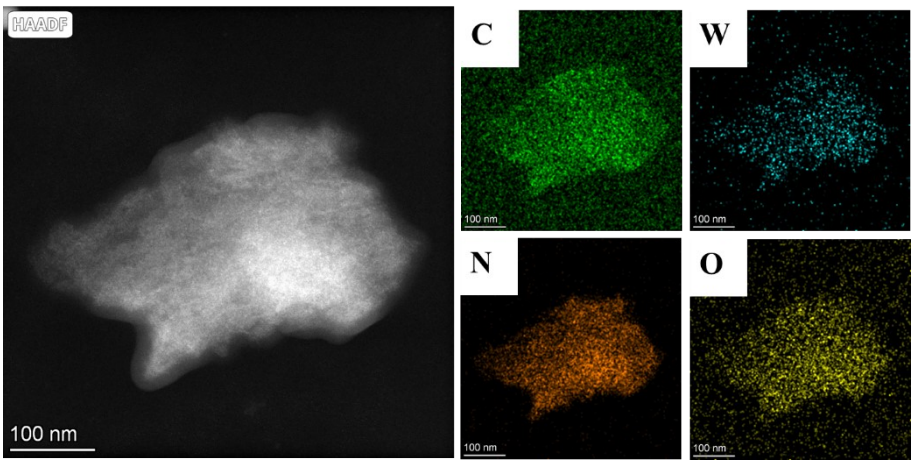

Figure S3. Energy-dispersive X-ray spectroscopy (EDS) mapping of the WCN material, scale bar: 100 nm. It can be clearly observed that signals of elements such as C, N, W, and O were present on the WCN material, indicating that WO_3 QDs have been successfully loaded onto the surface of the two-dimensional C_3N_3 material.

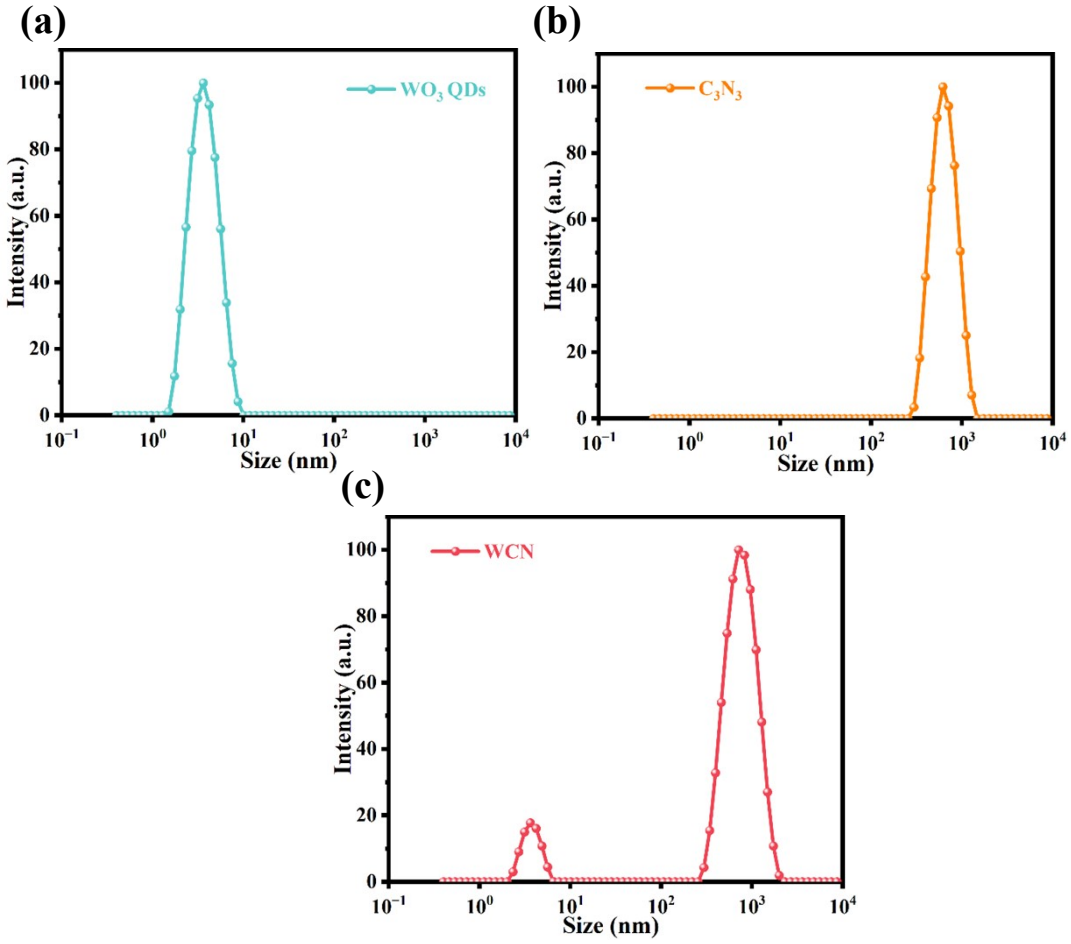

Figure S4. Particle size distribution in solutions of (a) WO_3 QDs, (b) C_3N_3, and (c) WCN as determined by DLS measurements. The particle size of WO_3 QDs exhibits a relatively narrow distribution with an average particle size of 5 nm, as illustrated in Figure S4 (a). It is observed that the particle size of WCN material has slightly increased compared to that of the exfoliated C_3N_3 comparing. However, since WO_3 QDs are deposited on the surface of C_3N_3 through self-assembled process, it is prone to fall off during the liquid sample preparation process, resulting in a small amount of WO_3 QDs signal appearing in WCN, which is consistent with the observations from the EDS measurement. This results in a minor presence of WO_3 QDs appearing in the WCN suspension, which is consistent with the observations from the EDS measurement.

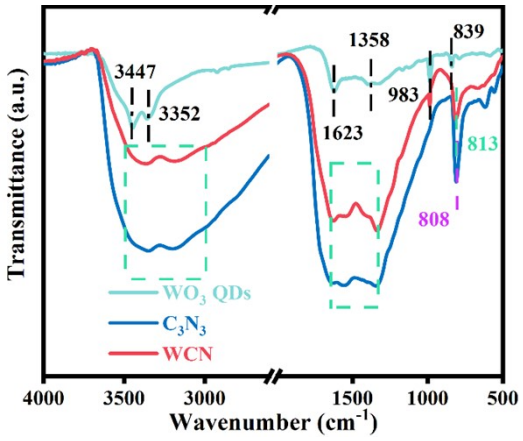

Figure S5. FTIR spectrum of the WO_3 QDs, C_3N_3, and WCN powder samples. From the spectrum, it can be observed that for the WO_3 QDs sample, the characteristic peaks at 3352 and 3447 cm^{-1} correspond to the stretching vibration peaks of the O-H bonds on the material surface, while the characteristic peaks at 1623 cm and 1358 cm^{-1} correspond to the bending vibration peaks of the O-H bonds on the material surface. It illustrates the characteristic peaks of WO_3 QDs at 839 and 983 cm^{-1}, which are assigned to the stretching vibrations of W-O-W and W-O bonds, respectively. For the C_3N_3 sample, the characteristic peaks in the range of 3000-3500 cm^{-1} correspond to the N-H stretching vibration peaks of -NH_2 groups around the C_3N_3 structure and the adsorbed water or terminal -OH bonds on the material surface. The characteristic peaks appearing in the range of 1300-1700 cm^{-1} are due to the vibration of the conjugated C=N bonds within the C_3N_3 structure, especially the characteristic peak near 808 cm^{-1}, which corresponds to the typical stretching vibration peak of the triazine ring within the C_3N_3 structure. Furthermore, compared with the characteristic vibration peak of C_3N_3 material, a weak characteristic vibration peak of WO_3 QDs appeared at 983 cm^{-1} in the WCN sample, indicating that WO_3 QDs were also successfully loaded onto the C_3N_3 carrier. It is worth noting that the typical stretching vibration peak of the triazine ring within the C_3N_3 structure shifted from 808 to 813 cm^{-1} in the WCN sample, demonstrating an interaction between WO_3 QDs and C_3N_3.

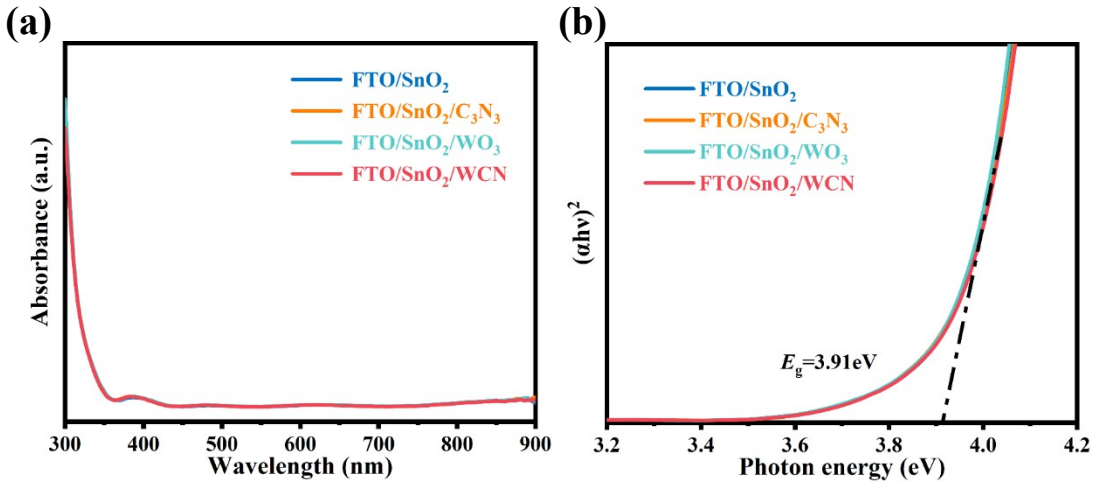

Figure S6. (a) UV-vis absorption spectrum and (b) the corresponding band gap maps of SnO_2 thin films before and after modification with different C_3N_3, WO_3 QDs, and WCN interface materials.

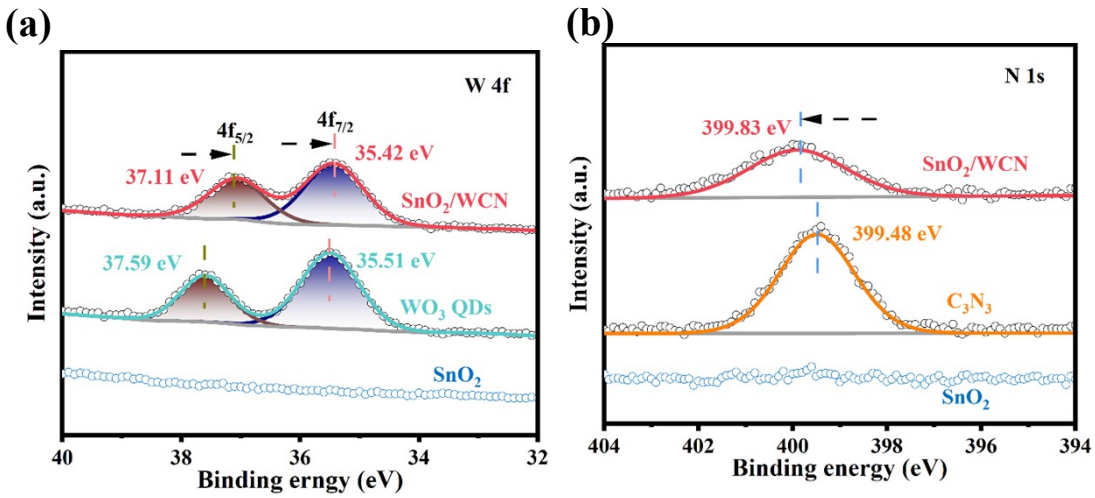

Figure S7. (a) W 4f high-resolution XPS spectra of SnO_2 film, WO_3 QDs powder, and SnO_2/WCN film. (b) N 1s high-resolution XPS spectra of SnO_2 film, C_3N_3 powder, and SnO_2/WCN film.

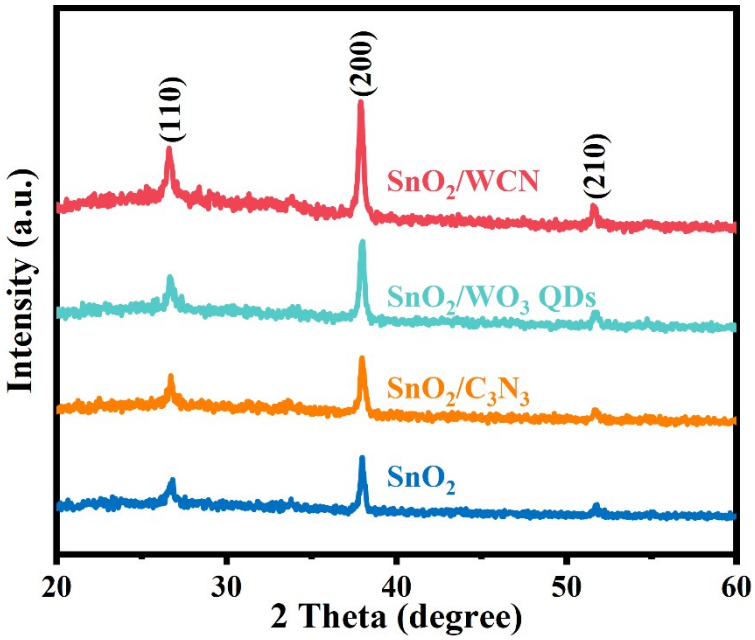

Figure S8. XRD patterns of the pristine SnO_2, SnO_2/C_3N_3, SnO_2/WO_3 QDs, and SnO_2/WCN films.

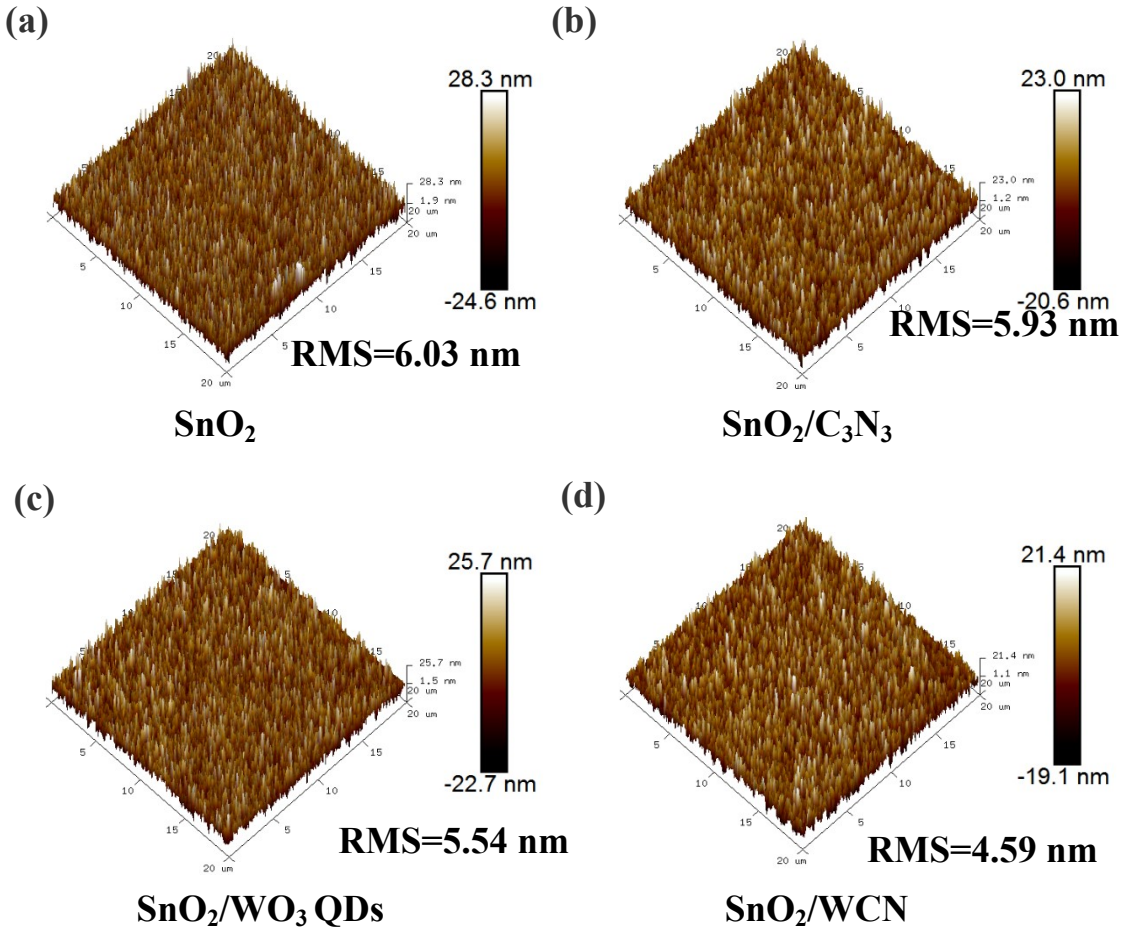

Figure S9. 3D AFM images of different films: (a) SnO_2, (b) SnO_2/C_3N_3, (c) SnO_2/WO_3 QDs, and (d) SnO_2/WCN. Scale bar, 4 μm

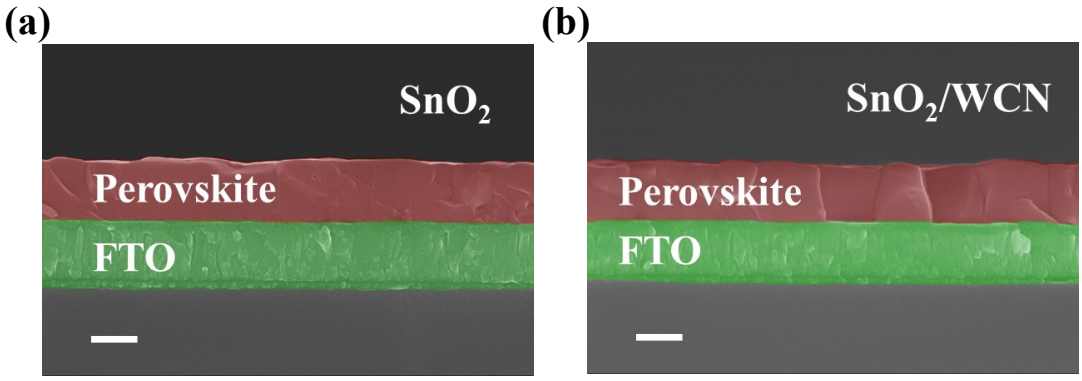

Figure S10. Cross-sectional SEM images of perovskite films deposited on (a) SnO_2 and (b) SnO_2/WCN substrates. Scale bar, 500 nm.

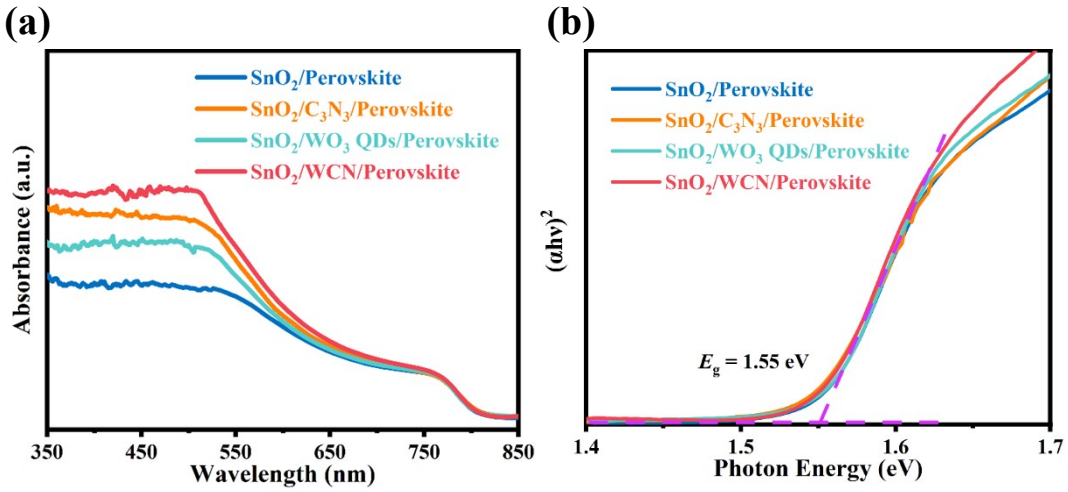

Figure S11. (a) UV-vis absorption spectra and (b) corresponding bandgap diagrams of perovskite thin films deposited on different substrates.

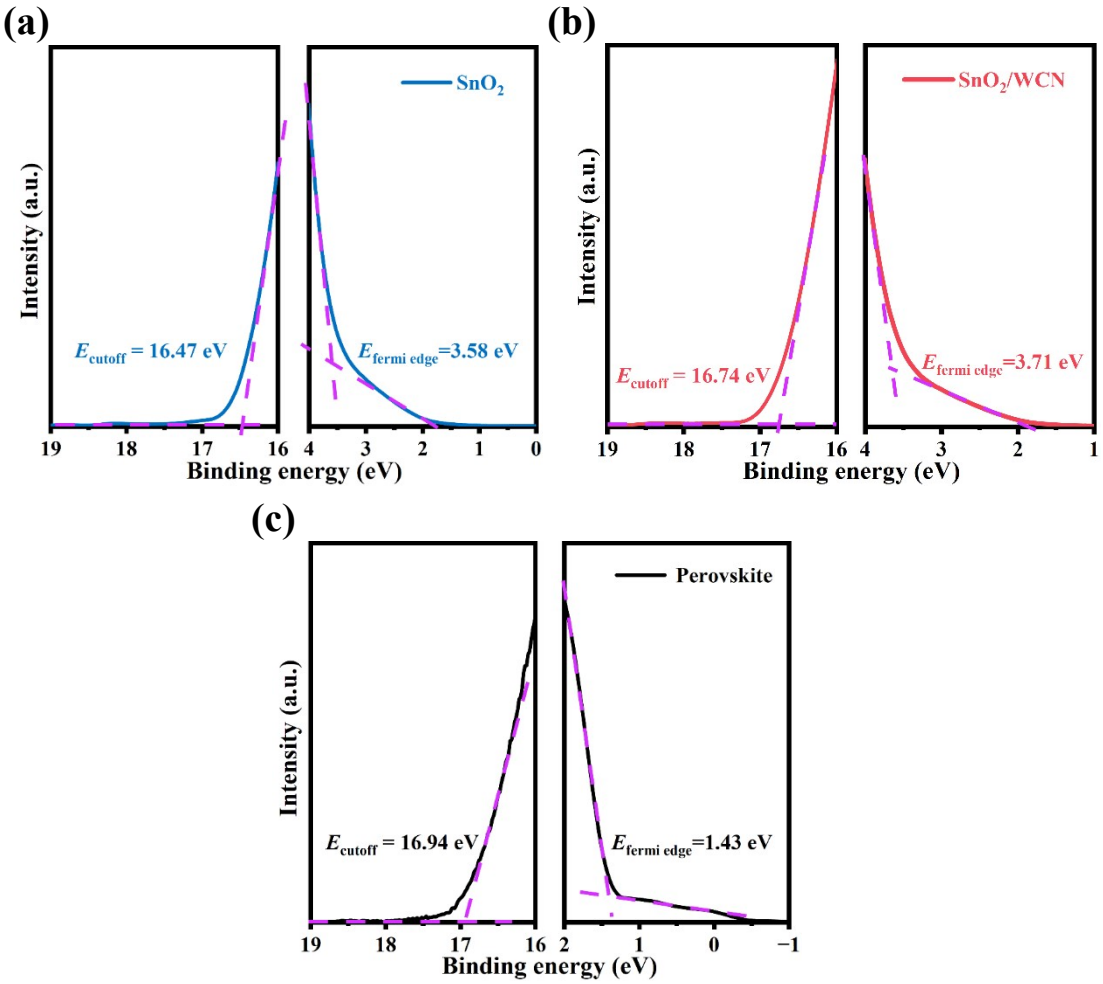

Figure S12 UPS spectra of secondary electron cutoff region and valence band region of (a) pristine SnO_2 film, (b) SnO_2/WCN film, and (c) perovskite film.

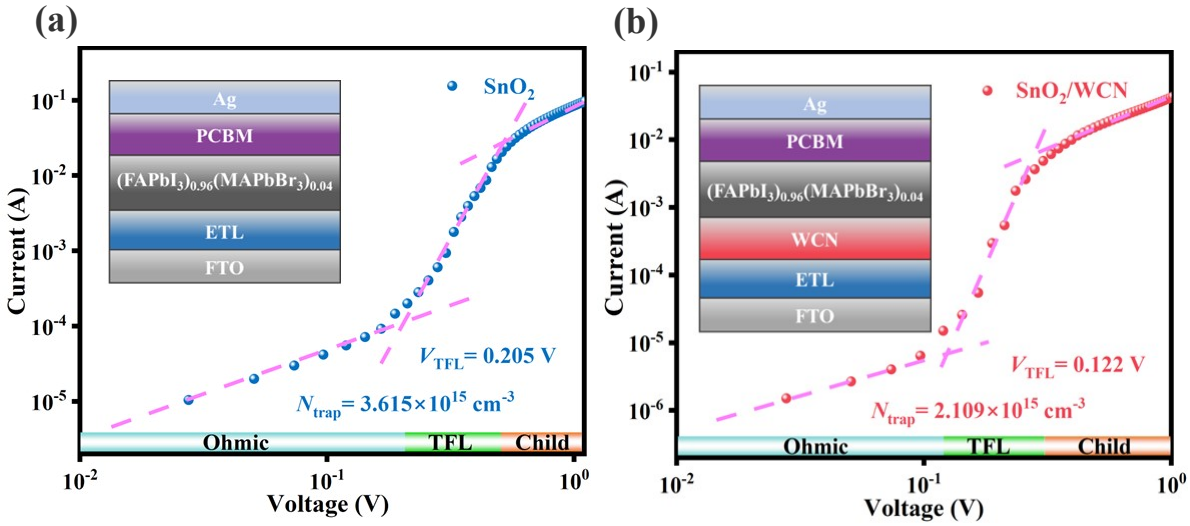

Figure S13. Dark *I-V* measurements with SCLC model based on the device structure of FTO/SnO_2 or SnO_2/WCN/perovskite/PCBM/Ag: (a) SnO_2 and (b) SnO_2/WCN. There are three regions in the dark *I-V* curves as the voltage increases, namely an ohmic region, a trap-filled limit region and a trap-free region. In the second region, the trap density (N_{trap}) is continuously filled until the trap-filled limit voltage (V_{TFL}) is reached, which can be obtained from the intersection point of the fitting lines in the first and second regions. The N_{trap} were calculated according to formula S1:

$$N_{trap} = \frac{2\varepsilon\varepsilon_0 V_{TFL}}{eL^2} \quad \text{(S1)}$$

Where e represents the elementary charge (1.60×10^{-19} C), L is the perovskite layer thickness (640 nm), ε and ε_0 are the relative dielectric constant and vacuum permittivity (8.85×10^{-12} F m^{-1}), respectively.[4, 5]

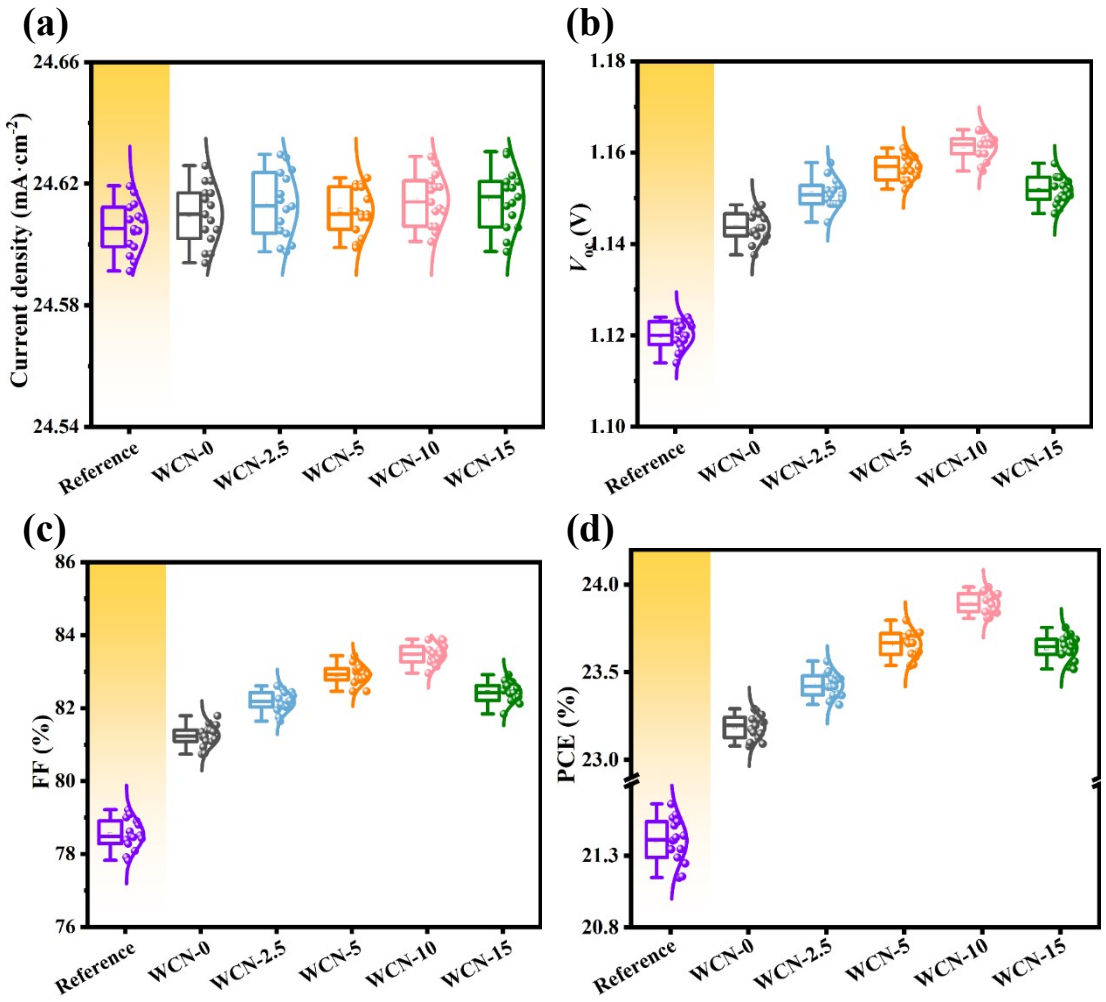

Figure S14. Statistics of key photovoltaic parameters obtained from the *J-V* characteristic of 15 devices modified with different concentrations of WCN: (a) J_{sc}, (b) V_{oc}, (c) FF, and (d) PCE. The SnO_2-based device without other treatment was used as the reference device. As the concentration of WCN increases from 0 to 0.10 mg·mL^{-1}, the performance parameters of the device improve correspondingly. However, with further increases in concentration, the performance of the PSC devices begins to decline. This decrease may be due to excessively high WCN concentrations negatively impacting the quality of the interface modification layer and the deposition of the perovskite film. Therefore, the optimal concentration of WCN was determined as 0.10 mg·mL^{-1} (abbreviated WCN-10, specifically 0.25 mg·mL^{-1} for C_3N_3 and 0.10 mg·mL^{-1} for WO_3 QDs) for the champion efficiency of PSCs.

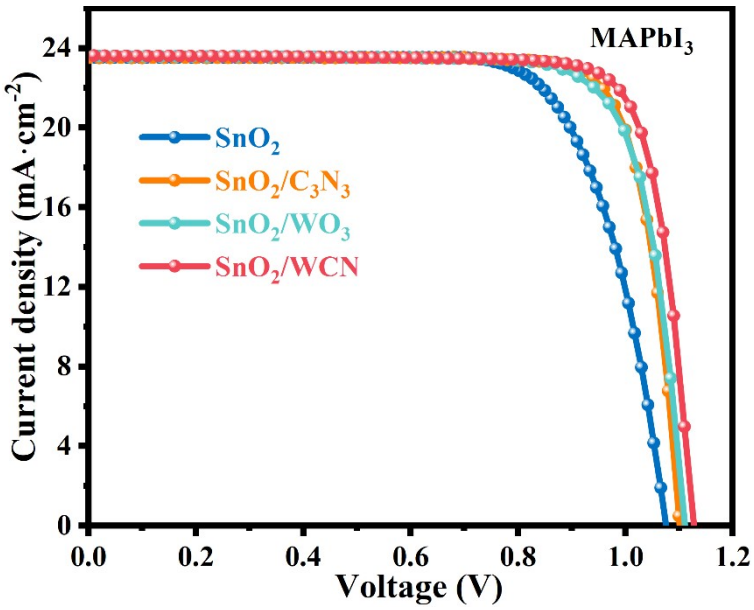

Figure S15. The *J-V* curves of the $MAPbI_3$-based PSCs under AM 1.5G illumination (100 mW cm^{-2}) with the pristine SnO_2, SnO_2/C_3N_3, SnO_2/WO_3 QDs, and SnO_2/WCN substrates, respectively.

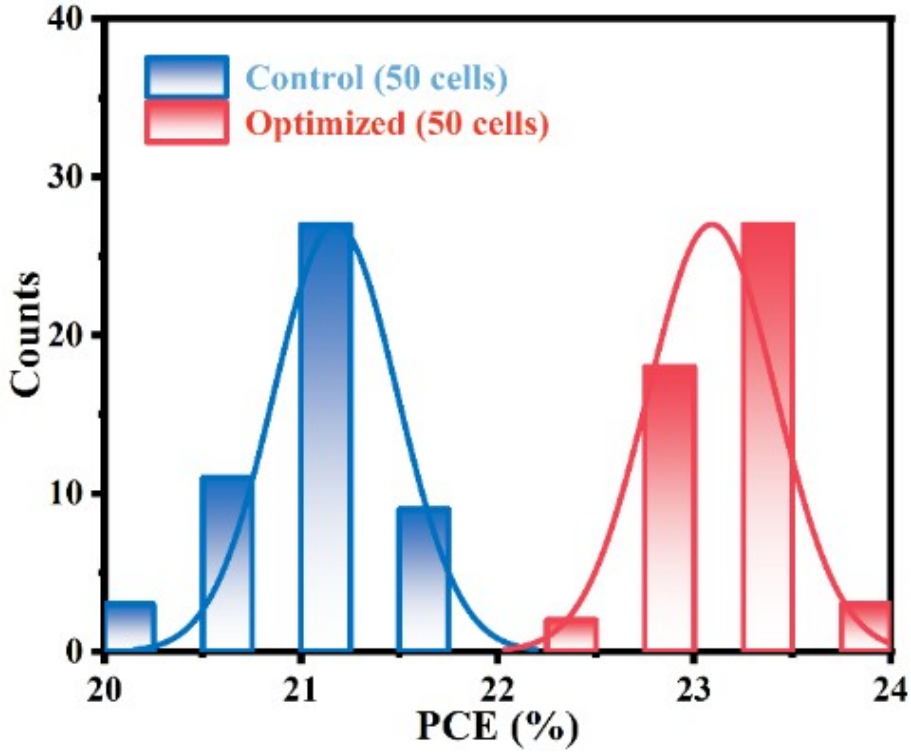

Figure S16. Histograms of PCE distribution among 50 control and optimized devices. Measurements were collected from 50 devices for each condition. The solid lines show Gaussian distribution fits for the PCE statistics. The bars represent the device count.

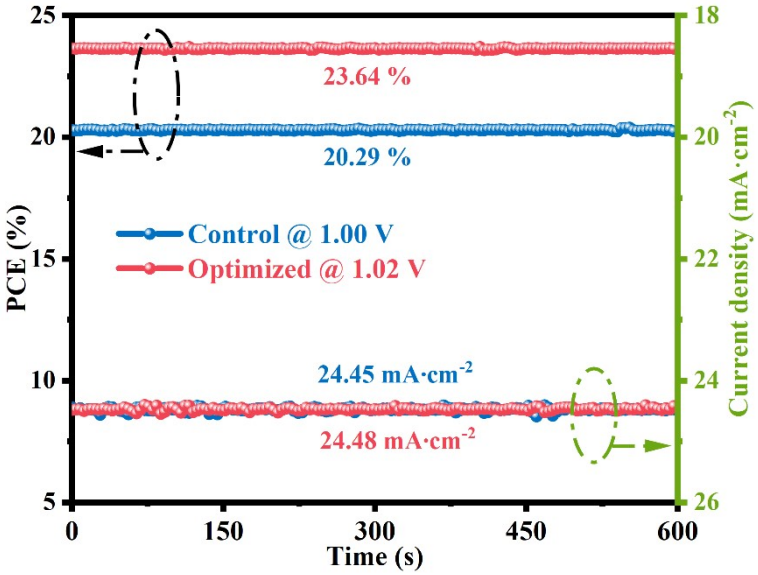

Figure S17. Steady-state photocurrent and PCE output curves of the control and optimized devices measured at a maximum power point.

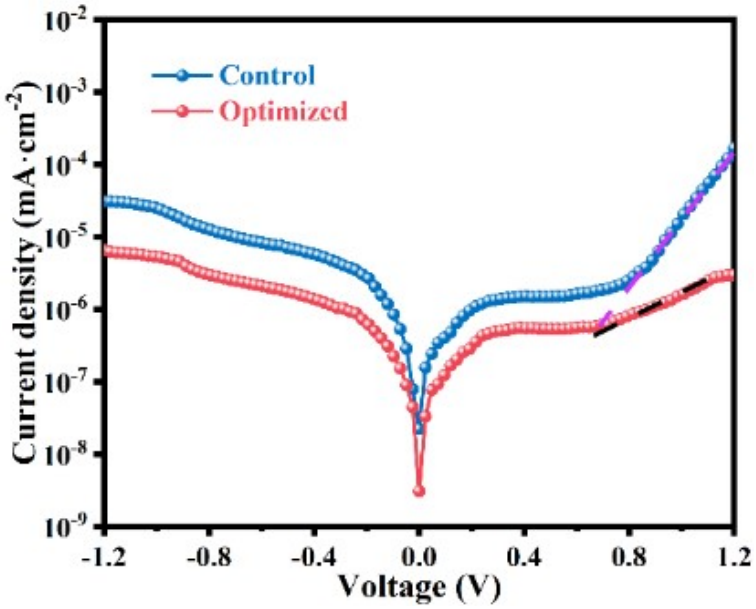

Figure S18. Dark *J-V* measurements of the control and optimized devices.

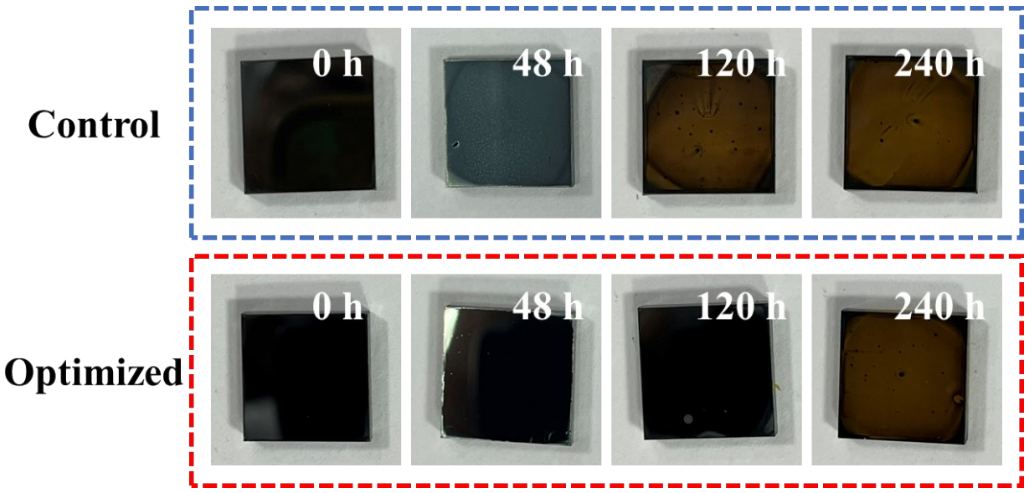

Figure S19. Evolution of perovskite films with and without WCN modified substrates of exposure time in an air environment.

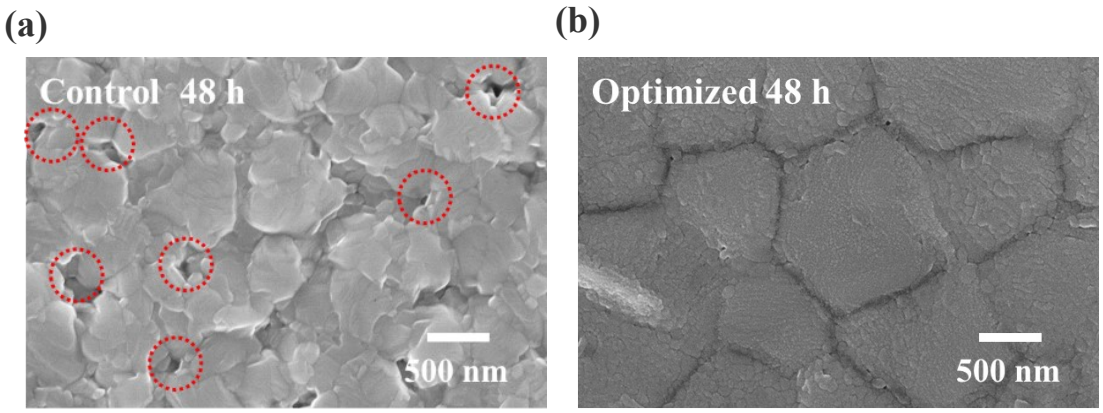

Figure S20. SEM images of the bottom surface of perovskite films deposited on (a) SnO_2 and (b) SnO_2/WCN substrates after being storage in an air for 48 h. Scale bar, 500 nm.

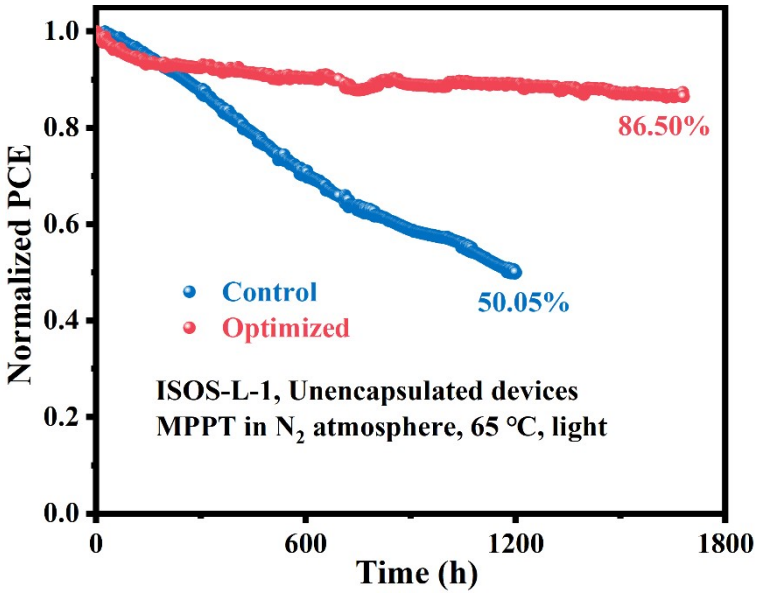

Figure S21. Operational stability of unencapsulated devices with MPPT under continuous 1-sunequivalent white-light LED illumination at 65 °C hot plate in N_2 atmosphere. The initial PCEs of the control and optimized devices used for the operational stability tests were 22.75% and 24.21%, respectively.

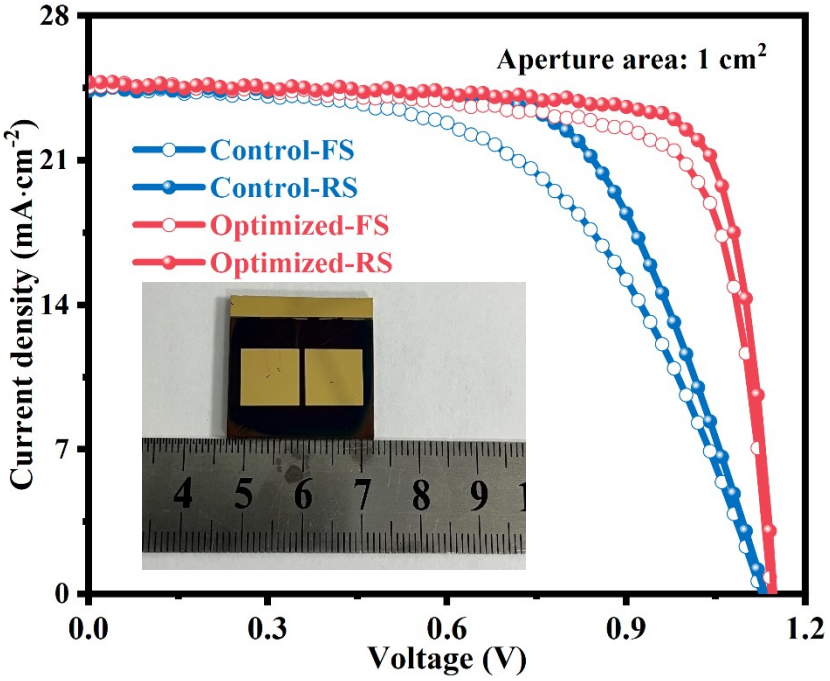

Figure S22. Forward and reverse scan *J-V* curves of control and optimized devices with area of 1 cm^2.

Table S1. Electrical conductivity of SnO_2, SnO_2/C_3N_3, SnO_2/WO_3 QDs, and SnO_2/WCN films.

Sample	Slope (*I*/*V*)	σ (mS·cm^{-1})
FTO/SnO_2/Au	0.06716	3.358×10^{-3}
FTO/SnO_2/C_3N_3/Au	0.08331	4.1655×10^{-3}
FTO/SnO_2/WO_3 QDs/Au	0.07575	3.7875×10^{-3}
FTO/SnO_2/WCN/Au	0.09307	4.6537×10^{-3}

The conductivities of the films calculated by the equations:

$$I = \sigma A L^{-1} \quad \text{(S2)}$$

where L is the thickness of ETL (30 nm) and A is the active area (0.06 cm^2).

Table S2. Electron mobility of SnO_2, SnO_2/C_3N_3, SnO_2/WO_3 QDs, and SnO_2/WCN films.

Sample	Slope ($J^{1/2}/V$)	μ ($cm^2 \cdot V^{-1} \cdot s^{-1}$)
FTO/SnO_2/PCBM/Ag	16.35834	5.237×10^{-3}
FTO/SnO_2/C_3N_3/PCBM/Ag	18.06145	6.384×10^{-3}
FTO/SnO_2/WO_3 QDs/PCBM/Ag	17.16469	5.766×10^{-3}
FTO/SnO_2/WCN/PCBM/Ag	19.15536	7.181×10^{-3}

The mobilities of the films were calculated by the Mott-Gurney equations:

$$J = \frac{9}{8}\varepsilon_0\varepsilon_r\mu\frac{V^2}{L^3} \quad \text{(S3)}$$

where J is current density, μ is free carrier mobility, ε_0 is permittivity of vacuum free space, ε_r is the dielectric constant of ETLs, V is the applied voltage, and L is the thickness of ETL (30 nm), respectively.[6]

Table S3. Energy band structure parameters of SnO_2, SnO_2/WCN, and perovskite films.

Sample	E_g (eV)	E_{cutoff} (eV)	$E_{fermi\ edge}$ (eV)	E_F (eV)	E_{VB} (eV)	E_{CB} (eV)
SnO_2	3.91	16.47	3.58	4.75	-8.33	-4.42
SnO_2/WCN	3.91	16.74	3.71	4.48	-8.19	-4.28
Perovskite	1.55	16.94	1.43	4.28	-5.71	-4.16

From these obtained values in Figure S8, the Fermi levels (E_F), valence band maxima (E_{VBM}), and conduction band minima (E_{CBM}), were calculated utilizing the following equation:

$$E_F = h\nu - E_{cutoff} \quad \text{(S4)}$$

$$E_{VBM} = E_F + E_{fermi} \quad \text{(S5)}$$

$$E_{CBM} = E_{VBM} - E_g \quad \text{(S6)}$$

Where $h\nu$ represents the UV photoelectron energy of 21.22 eV and E_g is the optical bandgap.[7]

Table S4. Fitting lifetime and amplitude parameters for TRPL testing of perovskite films with and without WCN interface modification.

Sample	A_1 (%)	τ_1 (ns)	A_2 (%)	τ_2 (ns)	τ_{ave} (ns)
SnO_2/Perovskite	21.9	140	78.1	184.6	174.8
SnO_2/WCN/Perovskite	16.4	160	83.6	89.9	101.4

The TRPL measured data were fitted using a biexponential decay model:

$$y(t) = A_1 exp\left(-\frac{t}{\tau_1}\right) + A_2 exp\left(-\frac{t}{\tau_2}\right) + y_0 \quad \text{(S7)}$$

And the average lifetime (τ_{ave}) was calculated via the weighted average of each decay component:

$$\tau_{ave} = \frac{\left(A_1\tau_1^2 + A_2\tau_2^2\right)}{A_1\tau_1 + A_2\tau_2} \quad \text{(S8)}$$

where A_1 and A_2 represent the amplitude factors of the fast-decay and slow-decay component, respectively. The fast decay time (τ_1) represents the rapid decay of photogenerated carriers from the perovskite absorber to ETL, the long decay time (τ_2) represents radiation recombination in the perovskite crystal phase, and y_0 is base line displacement constant.[8, 9]

Table S5. Photovoltaic parameters of PSC devices based on interface modification with different WCN concentrations.

Sample	PCE (%)	V_{oc} (V)	J_{sc} (mA·cm^{-2})	FF (%)
SnO_2 (Reference)	21.63 (21.51±0.15)	1.120 (1.120±0.003)	24.60 (24.61±0.02)	78.51 (78.54±0.42)
SnO_2/WCN-0	23.11 (23.19±0.07)	1.150 (1.149±0.003)	24.61 (24.61±0.02)	81.66 (81.24±0.29)
SnO_2/WCN-2.5	23.43 (23.43±0.07)	1.152 (1.151±0.003)	24.60 (24.61±0.02)	82.68 (82.17±0.27)
SnO_2/WCN-5.0	23.65 (23.65±0.075)	1.154 (1.157±0.003)	24.61 (24.611±0.01)	83.27 (82.92±0.27)
SnO_2/WCN-10	23.92 (23.89±0.06)	1.160 (1.161±0.003)	24.60 (24.62±0.01)	83.82 (83.47±0.28)
SnO_2/WCN-15	23.64 (23.64±0.07)	1.152 (1.152±0.003)	24.62 (24.62±0.02)	83.35 (82.43±0.28)

Table S6. Photovoltaic parameters of $(FAPbI_3)_{0.96}(MAPbBr_3)_{0.04}$ based PSCs modified with different interface materials.

Sample	PCE (%)	V_{oc} (V)	J_{sc} (mA·cm^{-2})	FF (%)
SnO_2	21.63	1.12	24.60	78.51
SnO_2/C_3N_3	23.11	1.15	24.61	81.66
SnO_2/WO_3	22.68	1.14	24.59	80.91
SnO_2/WCN	23.92	1.16	24.60	83.82

Table S7. Photovoltaic parameters of $MAPbI_3$ based PSCs modified with different interface materials.

Sample	PCE (%)	V_{oc} (V)	J_{sc} (mA·cm^{-2})	FF (%)
SnO_2	18.59	1.08	23.54	73.12
SnO_2/C_3N_3	21.15	1.10	23.52	81.75
SnO_2/WO_3	20.74	1.11	23.53	79.41
SnO_2/WCN	21.64	1.13	23.52	81.42

Table S8. Photovoltaic parameters of PSCs devices in the control group and optimization group under different scanning directions.

Sample	Scan	PCE (%)	V_{oc} (V)	J_{sc} (mA cm^{-2})	FF (%)	HI (%)
Control	Forward	19.91	1.09	24.57	74.34	7.74
	Reverse	21.58	1.12	24.55	78.48	
Optimized	Forward	23.47	1.16	24.58	82.31	1.72
	Reverse	23.88	1.16	24.59	83.72	

The hysteresis index (HI) was calculated by the formula:

$$HI = \frac{PCE_{RS} - PCE_{FS}}{PCE_{RS}} \times 100\% \quad \text{(S9)}$$

where PCE_{RS} and PCE_{FS} represent the PCE of the control and optimized PSCs with the reverse scan and forward scan, respectively.[8]

Table S9. Fitting parameters of EIS of PSCs in the control and optimization groups.

Sample	R_s (Ohm)	R_{tr} (Ohm)	R_{rec} (Ohm)
Control	17.48	758.7	1506.59
Optimized	12.45	390.7	3593.15

Table S10. The forward and reverse scan photovoltaic performance parameters for control and optimized PSCs (area = 1 cm^2).

Sample	Scan	PCE (%)	V_{oc} (V)	J_{sc} (mA cm^{-2})	FF (%)	HI (%)
Control	Forward	15.57	1.145	24.56	55.38	14.96
	Reverse	18.31	1.149	24.67	64.61	
Optimized	Forward	20.85	1.144	24.59	74.11	6.16
	Reverse	22.22	1.149	24.61	78.57	

The hysteresis index (HI) was calculated by the formula:

$$HI = \frac{PCE_{RS} - PCE_{FS}}{PCE_{RS}} \times 100\% \quad \text{(S9)}$$

where PCE_{RS} and PCE_{FS} represent the PCE of the control and optimized PSCs with the reverse scan and forward scan, respectively.

References

1. H. Min, D. Y. Lee, J. Kim, G. Kim, K. S. Lee, J. Kim, M. J. Paik, Y. K. Kim, K. S. Kim, M. G. Kim, T. J. Shin and S. Il Seok, *Nature*, 2021, **598**, 444-450.
2. Z. Li, J. Feng, J. Cao, J. Jin, Y. Zhou, D. Cao, Z. Liang, B. Zhu, M. Li, L. Zhao and S. Wang, *Energy Environ. Mater.*, 2023, **6**, e12283.
3. Q. Liu, C. Hu and X. Wang, *Applied Surface Science*, 2019, **480**, 404-409.
4. C. Zhang, H. Li, C. Gong, Q. Zhuang, J. Chen and Z. Zang, *Energy Environ. Sci.*, 2023, **16**, 3825-3836.
5. D. Cao, Z. Li, W. Li, K. Pei, X. Zhang, L. Wan, L. Zhao, A. Cherevan, D. Eder and S. Wang, *Mater. Chem. Front.*, 2023, **7**, 964-974.
6. X. Sun, Y. Li, D. Liu, R. Liu, B. Zhang, Q. Tian, B. Fan, X. Wang, Z. Li, Z. Shao, X. Wang, G. Cui and S. Pang, *Adv. Energy Mater.*, 2023, **13**, 2302191.
7. Y. Cao, J. Feng, M. Wang, N. Yan, J. Lou, X. Feng, F. Xiao, Y. Liu, D. Qi, Y. Yuan, X. Zhu and S. Liu, *Adv. Energy Mater.*, 2023, **13**, 2302103.
8. J. Xia, M. Sohail and M. K. Nazeeruddin, *Adv. Mater.*, 2023, **35**, 2211324.
9. C. Luo, G. Zheng, F. Gao, X. Wang, C. Zhan, X. Gao and Q. Zhao, *Nat. Photonics*, 2023, **17**, 856-864.